ACS APPLIED MATERIALS & INTERFACES

Research Article

www.acsami.org

Nb-Doped Rutile TiO_2: a Potential Anode Material for Na-Ion Battery

Hiroyuki Usui, Sho Yoshioka, Kuniaki Wasada, Masahiro Shimizu, and Hiroki Sakaguchi*

†Department of Chemistry and Biotechnology, Graduate School of Engineering, and Center for Research on Green Sustainable Chemistry, Tottori University, 4-101 Minami, Koyama-cho, Tottori 680-8552, Japan

Supporting Information

ABSTRACT: The electrochemical properties of the rutile-type TiO_2 and Nb-doped TiO_2 were investigated for the first time as Na-ion battery anodes. $Ti_{1-x}Nb_xO_2$ thick-film electrodes without a binder and a conductive additive were prepared using a sol−gel method followed by a gas-deposition method. The TiO_2 electrode showed reversible reactions of Na insertion/extraction accompanied by expansion/contraction of the TiO_2 lattice. Among the $Ti_{1-x}Nb_xO_2$ electrodes with x = 0−0.18, the $Ti_{0.94}Nb_{0.06}O_2$ electrode exhibited the best cycling performance, with a reversible capacity of 160 mA h g^{-1} at the 50th cycle. As the Li-ion battery anode, this electrode also attained an excellent rate capability, with a capacity of 120 mA h g^{-1} even at the high current density of 16.75 A g^{-1} (50C). The improvements in the performances are attributed to a 3 orders of magnitude higher electronic conductivity of $Ti_{0.94}Nb_{0.06}O_2$ compared to that of TiO_2. This offers the possibility of Nb-doped rutile TiO_2 as a Na-ion battery anode as well as a Li-ion battery anode.

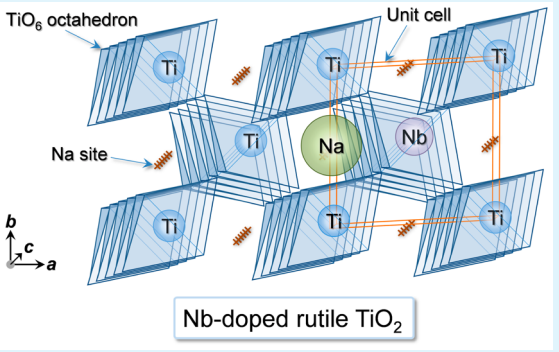

KEYWORDS: *rutile-type titanium oxide, Nb doping, Na-ion battery, Li-ion battery, gas deposition, thick-film electrode*

INTRODUCTION

As demands for renewable energy storage devices have rapidly grown, the sodium (Na)-ion battery (NIB) has drawn increasing attention because Na is an abundant and widespread resource in seawater in contrast to lithium (Li) for the Li-ion battery (LIB). The NIB is very similar to the LIB from the perspective of a rechargeable battery based on the transfer of alkali-metal ions between the electrode and electrolyte. On the other hand, the Na-ion volume is 2.4 times greater than that of the Li ion because Shannon's ionic radii of Na and Li are 102 and 76 pm, respectively. Because of the larger size of the charge carrier in a battery, the active materials and electrolytes of the NIB require a new material design different from that of the well-established LIB system. This is one of the most interesting features in basic research as well as a short-time task in NIB development. A great effort has been made for the development of active materials composed of rare-metal-free and low-cost elements. Some prospective cathode material candidates containing abundant transition metals have recently been developed. For instance, $NaFeO_2$,[1] $Na_x[Fe_{1/2}Mn_{1/2}]O_2$,[2] and $Na_2Fe_2(SO_4)_3$[3] are very promising active materials. On the basis of a previous study of anode materials, Komaba et al. revealed that a disordered carbon electrode exhibited a reversible capacity of 220 mA h g^{-1} and a stable cyclability for 100 charge−discharge cycles at a current density of 25 mA g^{-1}.[4] A practical application of the NIB, however, requires further advanced performance with regard to reversible capacity, cyclability, and rate capability.

The charge−discharge mechanism of anode materials can be basically classified into three types: (i) alloying/dealloying reaction; (ii) conversion reaction; (iii) insertion/extraction reaction. Because elemental phosphorus (P),[5] tin (Sn),[6−8] and antimony (Sb)[9,10] show alloying/dealloying reactions with Na and resulting high theoretical capacities (P, 2596 mA h g^{-1}; Sn, 847 mA h g^{-1}; Sb, 660 mA h g^{-1}), these elements and their compounds, such as NiP_3,[11] SnO,[12] and Cu_2Sb,[13] have been intensely studied. The important issues of their severe volume changes still remain to be resolved. The conversion reactions of Fe_3O_4[14] and FeS_2[15] also lead to high theoretical capacities of 926 and 893 mA h g^{-1}, respectively. Electrodes of this type, however, generally have problems of a low Coulombic efficiency for the first cycle and a high potential hysteresis. In terms of the insertion and extraction reactions into and from the crystal lattice, some titanium oxide based materials have attracted much attention. Although the theoretical capacities are not very large, the materials are very important for the NIB because a $Li_4Ti_5O_{12}$ anode[16] has been practically used for the LIB in electric vehicles. Reversible reactions of Na insertion/extraction have been reported for anatase TiO_2,[17−19] TiO_2(B),[20,21] $Na_2Ti_3O_7$,[22] and $Na_{2+x}Ti_6O_{13}$.[23] In contrast, there has been no study that tried to apply rutile TiO_2 to the NIB anode, to the best of the authors' knowledge. The reason is suggested to be the lower electrochemical activity of rutile as an active material than anatase TiO_2, which is well-known for the LIB anode.

Received: December 9, 2014
Accepted: March 10, 2015
Published: March 10, 2015

DOI: 10.1021/am508670z
ACS Appl. Mater. Interfaces 2015, 7, 6567−6573

Rutile TiO_2 has the most unique characteristics of Li^+ diffusion in some polymorphs of TiO_2; its diffusion coefficient along the *c* direction is approximately 10^{-6} cm^2 s^{-1}, while it is only 10^{-15} cm^2 s^{-1} in the *ab* plane. Because of its highly anisotropic diffusion, three-dimensional Li^+ diffusion is kinetically restricted in micrometer-sized rutile TiO_2, resulting in its poor anode property. Concerning this subject, Maier et al.[24] and Tarascon et al.[25] reported that rutile TiO_2 with size of several tens of nanometers exhibited enhanced reversible capacities and improved cycle stabilities as an LIB anode. We have also found that the anode performances of the TiO_2/silicon (Si) composite electrodes were considerably improved by uniformly coating the rutile TiO_2 particles with 10−50 nm sized Si particles.[26] The authors have proposed that a smooth Li^+ diffusion in rutile can be successfully exerted based on its nanostructure, thereby providing improved anode performance. This effect is also expected for the NIB anode. In this study, we applied the rutile TiO_2 particles to the NIB anode and investigated its Na-insertion/extraction property for the first time. In addition, we tried to enhance its anode performance by Nb doping into rutile TiO_2.

EXPERIMENTAL SECTION

Nb-doped TiO_2 particles were synthesized by a sol−gel method using hydrochloric acid (HCl; Wako Pure Chemical Industries, 35−37% assay) and titanium(IV) tetraisopropoxide [$Ti(OCH(CH_3)_2)_4$; Wako Pure Chemical Industries, 95%]. The synthetic conditions of this method have basically been optimized in our previous study.[26] First, 4 mL of HCl was diluted in 56 mL of deionized water in a round-bottomed flask. Next, 2 mL of $Ti(OCH(CH_3)_2)_4$ was dripped into the solution. Finally, niobium(V) ethoxide [$Nb(OC_2H_5)_5$; Wako Pure Chemical Industries, 99.9%] was added to the solution with vigorous stirring. The stirring process was maintained for 4 h at 55 °C and 1000 rpm. The resulting colloidal suspensions were centrifuged and washed with deionized water three times. The washed precipitates were dried under vacuum at 85 °C for 24 h and then heated at 400 °C in air for 4 h. White powders of the Nb-doped TiO_2 particles were obtained after heat treatment.

The crystal structure of the powders was confirmed by X-ray diffraction (XRD; Ultima IV, Rigaku) with Cu Kα radiation. The morphology of the powders was observed by field-emission scanning electron microscopy (FE-SEM; JSM-6701F, JEOL Ltd.). A Raman spectral analysis for the powders was conducted at room temperature by a Raman microscopy system (NanofinderFLEX, Tokyo Instruments, Inc.) using a Nd:YAG laser at a 532 nm wavelength.

Nb-doped TiO_2 thick-film electrodes were prepared by a gas deposition (GD) method.[27,28] This method does not require any binder and conductive material to prepare thick-film electrodes, which is a notable advantage to evaluate the original electrochemical property of an active material. In this study, GD was carried out by using a nozzle with 0.5 mm diameter. A current collector of a titanium (Ti) foil substrate with 20 μm thickness was set at a distance of 10 mm from the nozzle. A helium carrier gas with a purity of 99.9999% flowed at a differential pressure of 5.0×10^5 Pa. The compositions of the active material powders and thick-film electrodes were analyzed by an energy-dispersive X-ray fluorescence spectrometer (EDX-720, Shimadzu Co. Ltd.). The active material weights of the electrodes were within the range of 110−130 μg. The deposition areas of the active materials were approximately 0.79 cm^2. The thickness of the Nb-doped TiO_2 layer on the Ti substrate was estimated to be approximately 14 μm by observation using confocal scanning laser microscopy (VK-9700, Keyence).

For evaluation as the anode of the NIB, we assembled 2032-type coin cells consisting of the thick film as the working electrode, Na foil as the counter electrode, electrolyte, and glass fiber separator. The electrolytes used in this study were 1 M $NaClO_4$ dissolved in propylene carbonate (PC; $C_4H_6O_3$, Kishida Chemical Co., Ltd.). The GD and cell assembly were performed in a purge-type glovebox (Miwa MFG, DBO-2.5LNKPTS) filled with an argon atmosphere in which the oxygen concentration and dew point were below 1 ppm and −100 °C, respectively. Constant-current charge−discharge tests were carried out using an electrochemical measurement system (HJ-1001 SM8A, Hokuto Denko Co., Ltd.) in the potential range between 0.005 and 3.000 V versus Na/Na^+ at 303 K at a constant current density of 50 mA g^{-1} (0.15*C*). Ex situ XRD measurements were also carried out for a TiO_2 thick-film electrode during the first charge−discharge cycle. To prevent the electrode from reacting with air, it was protected by a polyimide film in the glovebox. For comparison, we synthesized anatase TiO_2 and anatase Nb-doped TiO_2 particles with sizes similar to that of the rutile TiO_2 particles by the sol−gel method. The electrode performances were measured for anatase TiO_2, anatase Nb-doped TiO_2, a commercial anatase TiO_2 (Wako Pure Chemical Industries, 98.5%), and a commercial rutile TiO_2 (Wako Pure Chemical Industries, 99%).

As the anode of the LIB, we assembled coin cells consisting of the Nb-doped TiO_2 electrode, Li foil, and an electrolyte of 1 M lithium bis(trifluoromethanesulfonyl)amide/PC. The charge−discharge tests were performed in the potential range between 1.000 and 3.000 V versus Li/Li^+ at 303 K at various current densities from 167.5 mA g^{-1} (0.5*C*) to 16.75 A g^{-1} (50*C*).

RESULTS AND DISCUSSION

The experimental results of the FE-SEM observations and Raman spectroscopic measurements indicate that the active material powders consisted of primary particles with sizes of 10−50 nm and have a rutile-type TiO_2 structure whether or not Nb was doped (see Figures S1 and S2 in the Supporting Information, SI). Figure 1 shows the XRD patterns obtained for

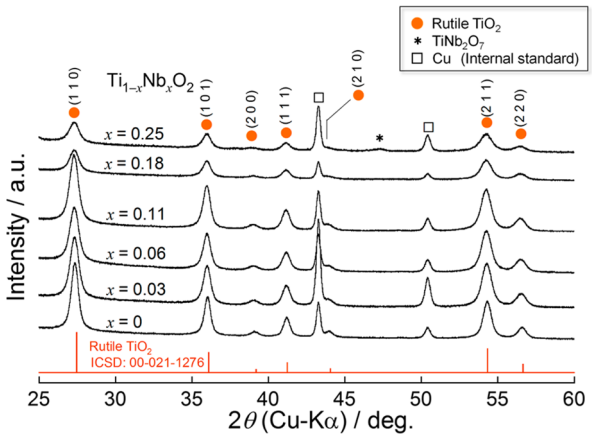

Figure 1. XRD patterns of $Ti_{1-x}Nb_xO_2$ active material powders synthesized by the sol−gel method.

the active material powders of $Ti_{1-x}Nb_xO_2$ with different Nb amounts *x* ranging from 0 to 0.25, synthesized via an optimized sol−gel method,[26] followed by a heat treatment at 400 °C in air. The resulting patterns were in good agreement with the rutile phase (Inorganic Crystal Structure Database, ICSD No. 00-021-1276). In the range of *x* from 0 to 0.18, a single phase of rutile TiO_2 was observed. When *x* was the maximum value of 0.25, a new crystal phase of a ternary compound ($TiNb_2O_7$) appeared in the pattern. Hereafter, we will focus on the active materials except for the powder with $x = 0.25$ because it contained an impurity phase unfavorable for discussion. It has been reported that Nb doping suppresses a coarsening of the TiO_2 grains[29] and that the origin is the reduced mobility of ionic oxygen.[30] Although the crystallinity was significantly degraded when *x* was 0.18 or higher, the crystalline sizes were

DOI: 10.1021/am508670z
ACS Appl. Mater. Interfaces 2015, 7, 6567−6573

estimated to be 13−16 nm up to $x = 0.11$ based on the Scherrer equation and basically did not depend on the Nb amount. In order to study the influence of the Nb amount on the crystal structure, we calculated the lattice parameters of rutile from the diffraction angles. The diffraction peak positions were precisely determined by a calibration using an internal standard of copper and by an analysis of a convolution-based profile fitting using a Gaussian function.

Figure 2 represents the lattice parameters of *a* and *c* in the $Ti_{1-x}Nb_xO_2$ powders. No remarkable change in *c* was observed

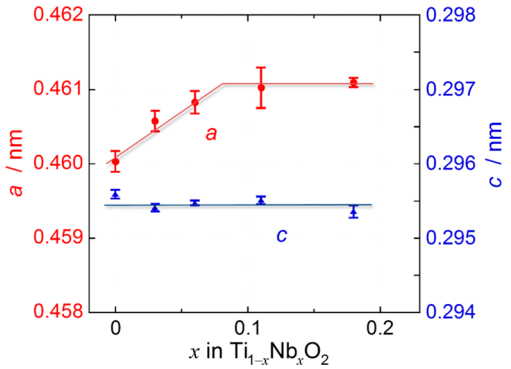

Figure 2. Lattice parameters *a* and *c* of $Ti_{1-x}Nb_xO_2$ active material powders as a function of the Nb amount *x*.

with an increase in the Nb amount. In contrast, *a* linearly increased with the Nb amount up to $x = 0.06$. This lattice expansion is attributed to a substitution of the Ti site in the rutile by Nb because the ionic radius of Nb^{5+} (64 pm) is greater than that of Ti^{4+} (60.5 pm). For higher Nb amounts of 0.11 and 0.18, no increase of *a* was observed. On the basis of these results, the excessive Nb possibly forms an impurity phase in the grain boundary between the TiO_2 crystallites, which causes an undesirable influence on Na^+ ion diffusion. We suggest that $Ti_{0.89}Nb_{0.11}O_2$ and $Ti_{0.82}Nb_{0.18}O_2$ presumably show anode properties inferior to those of other Nb-doped TiO_2 because of the reduced crystalline sizes and the impurity crystal phase formed by excess doping of Nb.

To evaluate the fundamental electrochemical properties of the NIB anode, we prepared thick-film electrodes without any binder and conductive material by a GD method.[27,28] Parts a and b of Figure 3 show the galvanostatic charge (sodiation) and discharge (desodiation) potential profiles of the $Ti_{1-x}Nb_xO_2$ thick-film electrodes for the 1st and 20th cycles. For the first cycle, there were high charge capacities greater than 300 mA h g^{-1} and Coulombic efficiencies lower than 35% in each electrode (Figure 3a). The irreversible capacities indicate the occurrence of side reactions, such as cathodic decomposition of the electrolyte and/or formation of a solid−electrolyte interface on the electrode. In particular, we suggest that decomposition of PC in the electrolyte mainly caused the low Coulombic efficiencies. Passerini et al. have reported that a PC-based electrolyte gives an anatase TiO_2 electrode a higher capacity compared with other electrolytes using solvents such as ethylene carbonate and dimethyl carbonate although its Coulombic efficiency is relatively low because of continuous decomposition of the PC-based electrolyte.[18] To suppress the irreversible capacity, the authors used fluoroethylene carbonate (FEC) as an electrolyte additive. It is suggested that FEC is first reduced on the anode surface, then polymerizes through the opening of a five-membered ring, and forms a stable protective layer containing NaF, sodium polycarbonate, and others. The protective layer can prevent further decompositions of electrolytes in successive cycles. In this study, the addition of 5 vol % FEC could considerably improve the reversibility of the capacity; the Coulombic efficiencies reached 99% and 100% at the 20th and 28th cycles, respectively (Figure S3 in the SI).

To find an electrode potential showing the Na-insertion/extraction reaction, we examined the charge−discharge profiles without FEC addition at the 20th cycle in which all of the electrodes exhibited relatively reduced side reactions and higher Coulombic efficiencies than approximately 80% (Figure S4 in the SI). In all of the electrodes, rounded potential shoulders were observed during the charge reaction at 0.1−0.7 V, the electrode potential referenced versus Na/Na^+, and during the discharge reaction at 0.5−1.0 V, as shown in Figure 3b. From the differential capacity plots of the profiles (Figure S5 in the SI), we found cathodic peaks at 0.7 and 0.1 V and an anodic peak at around 0.75 V. It is suggested that Na-insertion/extraction reactions occur at these potentials. However, a Na-insertion/extraction mechanism has never been explored, to the best of the authors' knowledge. To elucidate the mechanism, we performed ex situ XRD measurements for the electrodes during the charge−discharge reactions.

Figure 4 displays the ex situ XRD patterns collected during the charge−discharge process of the initial cycle of the TiO_2 electrode. A broad peak shoulder below 34° originates from a polyimide film covering the electrode surface for protection. During the charge process, the diffraction peaks of rutile TiO_2 shifted toward lower angles. Although the diffractions significantly weakened at 0.005 V, the (101) and (211) reflections still remained. During the discharge process, the

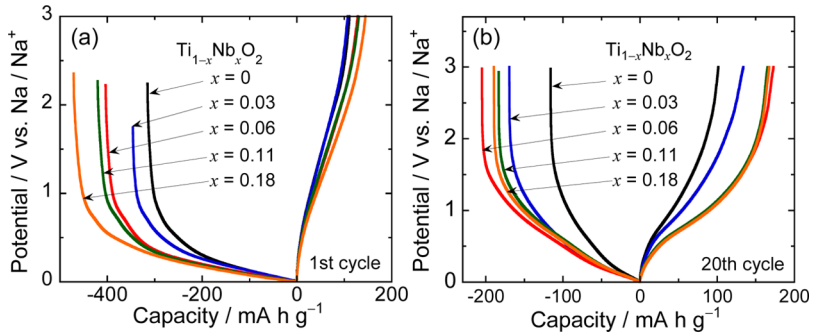

Figure 3. Galvanostatic charge (Na insertion) and discharge (Na extraction) profiles cycled between 0.005 and 3.0 V at a current density of 50 mA g^{-1} (0.15*C*) for the (a) 1st and (b) 20th cycles of $Ti_{1-x}Nb_xO_2$ thick-film electrodes.

DOI: 10.1021/am508670z
ACS Appl. Mater. Interfaces 2015, 7, 6567−6573

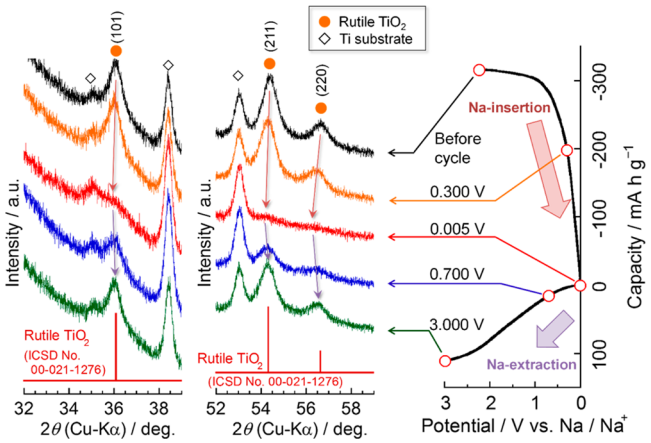

Figure 4. Ex situ XRD patterns of the TiO_2 electrode during the first cycle.

peak positions shifted toward higher angles associated with increasing diffraction intensities. The change in the patterns revealed that the crystal phase of rutile was basically maintained during the charge−discharge process and that there are reversible reactions of Na insertion and extraction into and from the crystal lattice of rutile TiO_2 although its crystallinity decreased once during the charge process. It is suggested that the crystal lattice is partially disordered by Na insertion because of its large ionic size. However, partial disordering is probably not an irreversible change because the crystallinity is partly recovered by Na extraction. Even after 10 cycles, the rutile crystal structure still remained, although the peak intensities were lowered (Figure S6 in the SI), demonstrating structural stability during Na insertion/extraction. Lattice expansion and contraction were clearly observed, as shown in Figure 5. It is

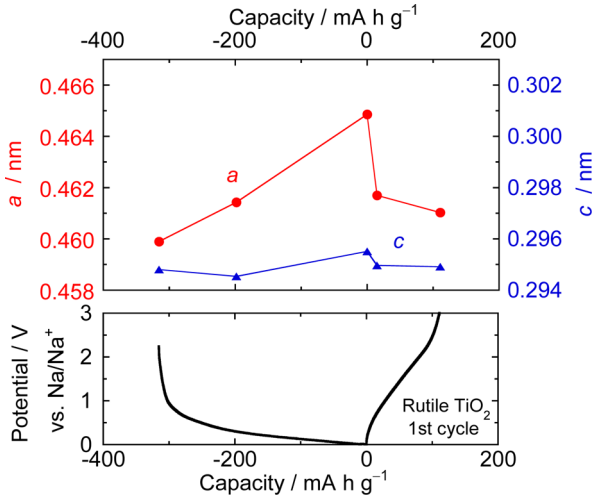

Figure 5. Changes in the lattice parameters of rutile TiO_2 during the first charge−discharge cycle.

considered that a conversion reaction possibly did not take place based on the following reasons: (i) the charge−discharge capacities were much lower than the theoretical capacity (1348 mA h g^{-1}) assumed by its conversion reaction; (ii) no diffraction peak of Ti metal or Na_2O was observed after charge−discharge; (iii) the diffraction peaks of rutile TiO_2 recovered after Na extraction. The lattice parameter c was not significantly changed during Na insertion/extraction. In contrast, the electrode showed about a 1.1% increase of a by Na insertion. The anisotropic lattice expansion has also been observed for Li-inserted rutile TiO_2.[25] The expansion rate of the unit cell volume was 2.4%, which is lower than 9.4% in a lithiated rutile TiO_2 ($Li_{0.6}TiO_2$) reported by Tarascon et al.[25] despite the larger ionic radius of Na^+ (102 pm) compared to Li^+ (76 pm). Taking into account the lower expansion rate, we speculate that Na insertion and diffusion in the lattice are more difficult than Li insertion and diffusion. Namely, a higher activation energy is probably required for Na insertion into rutile because of its larger ionic size. Guo et al.[31] has reported that electrochemical Na^+ diffusion in $Li_4Ti_5O_{12}$ is kinetically restricted compared to Li^+ diffusion because of its larger ionic size; the Na^+ diffusion coefficient of 10^{-16} cm^2 s^{-1} is much lower than the Li^+ diffusion coefficient of 10^{-12} cm^2 s^{-1}. The difference in the diffusion coefficients supports our speculation.

Figure 6a shows the cycling performances of the $Ti_{1-x}Nb_xO_2$ electrodes with various Nb amounts between x = 0 and 0.18. All of the electrodes showed a gradual increase in the discharge capacities until the 5th−15th cycles. It is suggested that the side reactions were gradually suppressed by the 5th−15th cycles. The discharge capacity increased with x. At x = 0.11 and 0.18, the electrode temporarily showed higher capacities in the initial several cycles and a greater capacity decay after the cycles compared to other electrodes. The capacity decay is presumably caused by the reduced crystalline sizes and the formation of an impurity crystal phase, as was already mentioned. Among all $Ti_{1-x}Nb_xO_2$, the electrode with x = 0.06 exhibited the best performance; the discharge capacity of 160 mA h g^{-1} was attained at the 50th cycle. The capacity of this electrode is comparable to that reported for a slurry electrode of anatase TiO_2 cycled at the current density of 37 mA g^{-1} (0.11C).[18] It is a noteworthy result that our rutile $Ti_{1-x}Nb_xO_2$ electrode delivered a comparable performance even though its active material layer is a thick film of approximately 14 μm and does not contain any conductive material and binder. There are two possible mechanisms for the improved performance by Nb doping into TiO_2, i.e., an increasing width of the Na^+ diffusion path along the c axis and an enhancement of its electronic conductivity. We assumed that the width of the diffusion path is an interstitial space between neighboring TiO_6 octahedra in tetragonal rutile structure because Na ions diffuse in the direction along [001] of the structure. Consequently, the widths of TiO_2 and $Ti_{0.94}Nb_{0.06}O_2$ were simply estimated to be 0.2300 and 0.2304 nm as half-values of the lattice parameters a obtained by XRD analysis. Because this difference in the width is much smaller than the diameter of Na^+ (0.204 nm), we speculate that the change in the electronic conductivity is more dominant than the increase in the width of the Na^+ diffusion path. In fact, we confirmed that TiO_2 and $Ti_{0.94}Nb_{0.06}O_2$ showed electronic resistivities of 2.6×10^5 and 2.1×10^2 Ω cm, respectively, by an electrical resistance measurement under a uniaxial press of active material powders. Figure 6b compares the rate capability of the $Ti_{1-x}Nb_xO_2$ electrodes with x = 0, 0.03, and 0.06. The rate capability was improved with increasing x, suggesting that the electrode can undergo charge−discharge at a higher current density because of a drastic increase in the conduction electron density by Nb doping into TiO_2. These results lead to the conclusion that improvements in the cycling performance and rate capability from x = 0 to 0.06 are attributed to a 3 orders of magnitude higher electronic conductivity of $Ti_{0.94}Nb_{0.06}O_2$ compared to TiO_2. The increased conductivity can enhance

DOI: 10.1021/am508670z
ACS Appl. Mater. Interfaces 2015, 7, 6567−6573

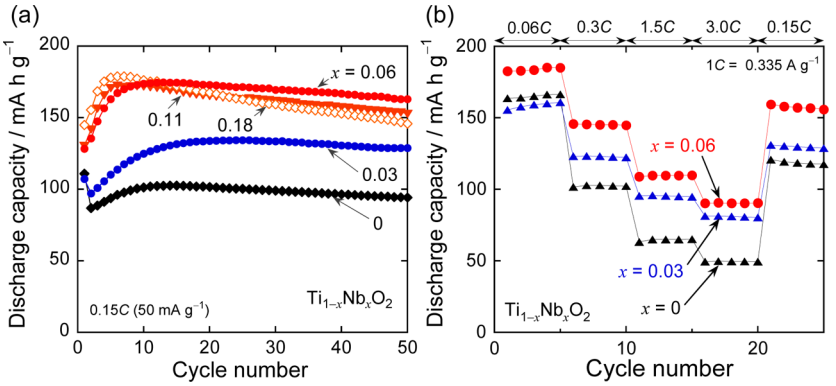

Figure 6. (a) Cycling performances of the rutile $Ti_{1-x}Nb_xO_2$ thick-film electrodes cycled at 50 mA g^{-1} (0.15C). (b) Rate capability of the $Ti_{1-x}Nb_xO_2$ electrodes under various rates from 20 mA g^{-1} (0.06C) to 1.0 A g^{-1} (3.0C).

the reaction efficiency of charge transfer of Na ions on the electrode surface because the number of electrons reaching the surface per unit time is increased in the charge process because of Nb doping. This causes an increase in the charge−discharge capacities.

Possible occupation sites of Na in a Nb-doped rutile TiO_2 structure are suggested, as illustrated in Figure 7. In principle, the rutile TiO_2 structure has two kinds of accommodation sites for Li: tetrahedral sites formed by TiO_6 octahedra sharing edges and octahedral sites built from corner-sharing of the octahedra. It has been reported that the accommodation of Li is more energetically preferable into the octahedral site because of its larger space than that of the tetrahedral site.[32] We consider that Na also preferably occupies the octahedral site for the same reason. Na insertion results in strong distortion of the lattice along the *ab* in-plane direction,[32] leading to anisotropic lattice expansion, as shown in Figure 5.

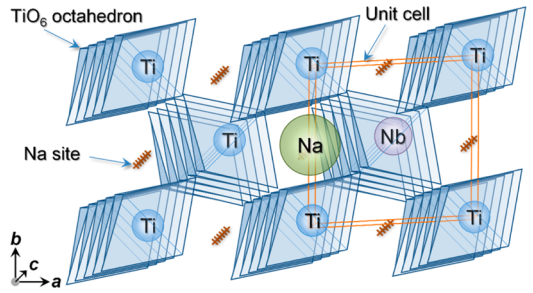

Figure 7. Possible occupation sites of Na in a Nb-doped rutile TiO_2 structure. Na probably occupies an octahedral oxygen-coordinated interstital site. Na^+ insertion results in strong distortion of the lattice along the *ab* in-plane direction, leading to anisotropic lattice expansion, as shown in Figure 5. Nb atoms randomly substitute for Ti atoms.

From the viewpoint of a rechargeable battery based on insertion/extraction of alkali-metal ions, we compared the anode properties of the NIB and LIB anodes. Parts a and b of Figure 8 present the cycling performances as the NIB anode and variation in the discharge capacities as the LIB anode cycled at various current densities. For comparison, we evaluated the anode properties for the thick-film electrodes of sol−gel-synthesized anatase-type TiO_2 (5−30 nm size), Nb-doped anatase (5−10 nm), commercial rutile TiO_2 (100−200 nm), and commercial anatase TiO_2 (70−200 nm). These figures show two similarities between the NIB and LIB anodes. One is improvement of the anode performances by reducing the particle size of the rutile and anatase TiO_2. The authors suggest that an essential mechanism of this size effect is the efficient insertion reaction into the inner part of the TiO_2 particle due to the reduced particle size close to its crystalline size. The size effect of rutile TiO_2 was less drastic in the NIB compared to the LIB. This comes from a slower diffusion of Na ions in the rutile. Na diffusion in the narrow channels of aspinel

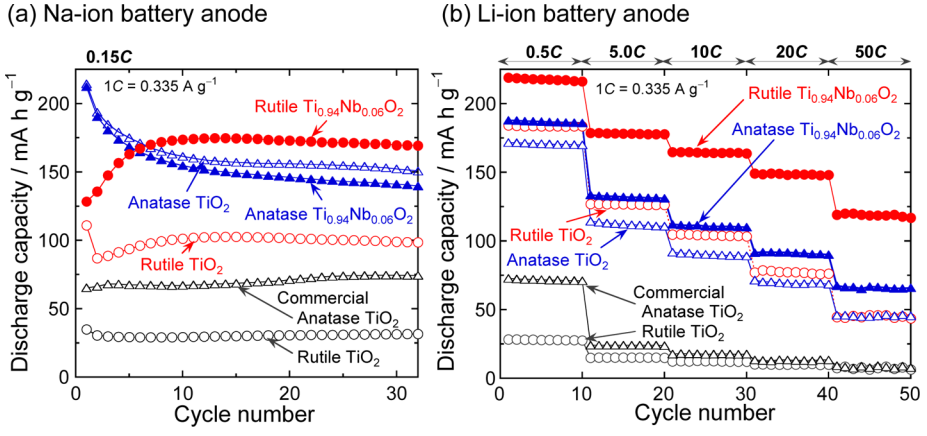

Figure 8. Performances of thick-film electrodes consisting of $Ti_{1-x}Nb_xO_2$ with rutile and anatase structure as (a) the NIB anode and (b) the LIB anode. For comparison, the figures show the results for thick-film electrodes of commercial rutile and anatase TiO_2.

DOI: 10.1021/am508670z
ACS Appl. Mater. Interfaces 2015, 7, 6567−6573

$Li_4Ti_5O_{12}$ shows a much lower diffusion coefficient and an energy penalty with a 0.7 V lower plateau voltage on account of the larger cation size in relation to Li diffusion.[31] In our experiments also, an about 0.7 V lower potential was also observed for Na insertion into the rutile (Figure S7 in the SI). These results show that a further high performance as the NIB can be achieved by an anode material with a broader channel size such as the hollandite-type TiO_2 or transition-metal-doped rutile. For instance, cerium (ionic radius of Ce^{3+} = 101 pm) is a promising dopant because its channel size and electrical conductivity can be simultaneously increased by doping. The other similarity is the increase in the discharge capacities of rutile TiO_2 by Nb doping. With respect to anatase TiO_2 as the NIB, the cyclability was not improved by Nb doping, which may be due to a slower kinetics of Na^+ diffusion in anatase compared to that in rutile. However, a detailed study on the difference in the anode properties between the anatase and rutile lies outside the scope of this brief paper. We will investigate the difference in the anode properties in a future study. As the LIB anode, the $Ti_{0.94}Nb_{0.06}O_2$ electrode also showed an excellent high-rate performance; a reversible capacity of 120 mA h g^{-1} was achieved even at the high current density of 16.75 A g^{-1} (50C). Therefore, these results demonstrated that the Nb-doped rutile TiO_2 is a promising anode material not only for the LIB but also for the NIB as a conductive-additive-free active material.

CONCLUSIONS

We reported for the first time the electrochemical properties of the Nb-doped rutile TiO_2 ($Ti_{1-x}Nb_xO_2$) as the NIB anode. Nb was successfully doped into rutile TiO_2 in the range from x = 0 to 0.06 by the sol–gel method. Ex situ XRD results revealed reversible reactions of Na insertion and extraction into and from the rutile TiO_2 lattice during the charge–discharge processes. Among the $Ti_{1-x}Nb_xO_2$ electrodes with x = 0–0.18, the $Ti_{0.94}Nb_{0.06}O_2$ electrode exhibited the best cycling performance with the reversible capacity of 160 mA h g^{-1} at the 50th cycle. In addition, it showed an improved rate capability. As the LIB anode, the electrode also attained an excellent rate capability with a capacity of 120 mA h g^{-1} even at the high-rate charge–discharge of 16.75 A g^{-1} (50C). These improved performances are mainly attributed to the 3 orders of magnitude higher electronic conductivity of $Ti_{0.94}Nb_{0.06}O_2$ compared to TiO_2. These results suggest that Nb-doped TiO_2 is an attractive candidate as a conductive-additive-free active material for the NIB anode as well as for the LIB anode.

ASSOCIATED CONTENT

Supporting Information

FE-SEM images, Raman spectra, Coulombic efficiency, ex situ XRD patterns, and initial charge–discharge curves. This material is available free of charge via the Internet at http://pubs.acs.org.

AUTHOR INFORMATION

Corresponding Author

*E-mail: sakaguch@chem.tottori-u.ac.jp. Tel./Fax: +81-857-31-5265.

Notes

The authors declare no competing financial interest.

ACKNOWLEDGMENTS

This work has been partially supported by a Japan Society for the Promotion of Science KAKENHI Grant-in-Aid for Scientific Research (B) (Grant 24350094). A part of this work was supported by the Japan Association for Chemical Innovation and the Kyoto Technoscience Center. The authors thank reviewers of this article for their helpful suggestions and comments.

REFERENCES

(1) Zhao, J.; Zaho, L.; Dimon, N.; Okada, S.; Nishida, T. Electrochemical and Thermal Properties of α-$NaFeO_2$ Cathode for Na-Ion Batteries. *J. Electrochem. Soc.* **2013**, *160*, A3077–A3081.

(2) Yabuuchi, N.; Iwatate, J.; Nishikawa, H.; Hitomi, S.; Okuyama, R.; Usui, R.; Yamada, Y.; Komaba, S. P2-type $Na_x[Fe_{1/2}Mn_{1/2}]O_2$ Made from Earth-Abundant Elements for Rechargeable Na Batteries. *Nat. Mater.* **2012**, *11*, 512–517.

(3) Barpanda, P.; Oyama, G.; Nishimura, S.; Chung, S.-C.; Yamada, A. A 3.8-V Earth-Abundant Sodium Battery Electrode. *Nat. Commun.* **2014**, *5*, 4358–1–8.

(4) Komaba, S.; Murata, W.; Ishikawa, T.; Yabuuchi, N.; Ozeki, T.; Nakayama, T.; Ogata, A.; Gotoh, K.; Fujiwara, K. Electrochemical Na Insertion and Solid Electrolyte Interphase for Hard-Carbon Electrodes and Application to Na-Ion Batteries. *Adv. Funct. Mater.* **2011**, *21*, 3859–3867.

(5) Qian, J.; Wu, X.; Cao, Y.; Ai, X.; Yang, H. High Capacity and Rate Capability of Amorphous Phosphorus for Sodium Ion Batteries. *Angew. Chem.* **2013**, *125*, 4731–4734.

(6) Wang, J. W.; Liu, X. H.; Mao, S. X.; Huang, J. Y. Microstructural Evolution of Tin Nanoparticles during In Situ Sodium Insertion and Extraction. *Nano Lett.* **2012**, *12*, 5897–5902.

(7) Komaba, S.; Matsuura, Y.; Ishikawa, T.; Yabuuchi, N.; Murata, W.; Kuze, S. Redox Reaction of Sn-Polyacrylate Electrodes in Aprotic Na Cell. *Electrochem. Commun.* **2012**, *21*, 65–68.

(8) Yamamoto, T.; Nohira, T.; Hagiwara, R.; Fukunaga, A.; Sakai, S.; Nitta, K.; Inazawa, S. Charge–Discharge Behavior of Tin Negative Electrode for a Sodium Secondary Battery Using Intermediate Temperature Ionic Liquid Sodium Bis(fluorosulfonyl)amide–Potassium Bis(fluorosulfonyl)amide. *J. Power Sources* **2012**, *217*, 479–484.

(9) Darwiche, A.; Marino, C.; Sougrati, M. T.; Fraisse, B.; Stievano, L.; Monconduit, L. Better Cycling Performances of Bulk Sb in Na-Ion Batteries Compared to Li-Ion Systems: An Unexpected Electrochemical Mechanism. *J. Am. Chem. Soc.* **2012**, *134*, 20805–20811.

(10) Wu, L.; Hu, X.; Qian, J.; Pei, F.; Wu, F.; Mao, R.; Ai, X.; Yang, H.; Cao, Y. Sb–C Nanofibers with Long Cycle Life as an Anode Material for High-Performance Sodium-Ion Batteries. *Energy Environ. Sci.* **2014**, *7*, 323–328.

(11) Fullenwarth, J.; Soares, A.; Donnadieu, B.; Monconduit, L. NiP_3: a Promising Negative Electrode for Li- and Na-Ion Batteries. *J. Mater. Chem. A* **2014**, *2*, 2050–2059.

(12) Shimizu, M.; Usui, H.; Sakaguchi, H. Electrochemical Na-Insertion/Extraction Properties of SnO Thick-Film Electrodes Prepared by Gas-Deposition. *J. Power Sources* **2014**, *248*, 378–382.

(13) Nam, D.-H.; Hong, K.-S.; Lim, S.-J.; Kwon, H.-S. Electrochemical Synthesis of a Three-Dimensional Porous Sb/Cu_2Sb Anode for Na-Ion Batteries. *J. Power Sources* **2014**, *247*, 423–427.

(14) Hariharan, S.; Saravanan, K.; Ramar, V.; Balaya, P. A Rationally Designed Dual Role Anode Material for Lithium-Ion and Sodium-Ion Batteries: Case Study of Eco-friendly Fe_3O_4. *Phys. Chem. Chem. Phys.* **2013**, *15*, 2945–2953.

(15) Kitajou, A.; Yamaguchi, J.; Hara, S.; Okada, S. Discharge/Charge Reaction Mechanism of a Pyrite-Type FeS_2 Cathode for Sodium Secondary Batteries. *J. Power Sources* **2014**, *247*, 391–395.

(16) Ohzuku, T.; Ueda, A.; Yamamoto, N. Zero-Strain Insertion Material of $Li[Li_{1/3}Ti_{5/3}]O_4$ for Rechargeable Lithium Cells. *J. Electrochem. Soc.* **1995**, *142*, 1431–1435.

(17) Kim, K.-T.; Ali, G.; Chung, K. Y.; Yoon, C. S.; Yashiro, H.; Sun, Y.-K.; Lu, J.; Amine, K.; Myung, S.-T. Anatase Titania Nanorods as an

DOI: 10.1021/am508670z
ACS Appl. Mater. Interfaces 2015, 7, 6567–6573

Intercalation Anode Material for Rechargeable Sodium Batteries. *Nano Lett.* **2014**, *16*, 412−416.
(18) Wu, L.; Buchholz, D.; Bresser, D.; Chagas, G. L.; Passerini, S. Anatase TiO_2 Nanoparticles for High Power Sodium-Ion Anodes. *J. Power Sources* **2014**, *251*, 379−385.
(19) Oh, S.-M.; Hwang, J.-Y.; Yoon, C. S.; Lu, J.; Amine, K.; Belharouak, I.; Sun, Y.-K. High Electrochemical Performances of Microsphere C-TiO_2 Anode for Sodium-Ion Battery. *ACS Appl. Mater. Interfaces* **2014**, *6*, 11295−11301.
(20) Huang, J. P.; Yuan, D. D.; Zhang, H. Z.; Cao, Y. L.; Li, G. R.; Yang, H. X.; Gao, X. P. Electrochemical Sodium Storage of TiO_2(B) Nanotubes for Sodium Ion Batteries. *RSC Adv.* **2013**, *3*, 12593−12603.
(21) Yan, Z.; Liu, L.; Tan, J.; Zhou, Q.; Huang, Z.; Xia, D.; Shu, H.; Yang, X.; Wang, X. One-Pot Synthesis of Bicrystalline Titanium Dioxide Spheres with a Core-Shell Structure as Anode Materials for Lithium and Sodium Ion Batteries. *J. Power Sources* **2014**, *269*, 37−45.
(22) Senguttuvan, P.; Rousse, G.; Seznec, V.; Tarascon, J.-M.; Palacín, M. R. $Na_2Ti_3O_7$: Lowest Voltage Ever Reported Oxide Insertion Electrode for Sodium Ion Batteries. *Chem. Mater.* **2011**, *23*, 4109−4111.
(23) Shen, K.; Wagemaker, M. $Na_{2+x}Ti_6O_{13}$ as Potential Negative Electrode Material for Na-Ion Batteries. *Inorg. Chem.* **2014**, *53*, 8250−8256.
(24) Hu, Y.-S.; Kienle, L.; Guo, Y.-G.; Maier, J. High Lithium Electroactivity of Nanometer-Sized Rutile TiO_2. *Adv. Mater.* **2006**, *18*, 1421−1426.
(25) Baudrin, E.; Cassaignon, S.; Koelsch, M.; Jolivet, J.-P.; Dupont, L.; Tarascon, J.-M. Structural Evolution during the Reaction of Li with Nano-Sized Rutile Type TiO_2 at Room Temperature. *Electrochem. Commun.* **2007**, *9*, 337−342.
(26) Usui, H.; Wasada, K.; Shimizu, M.; Sakaguchi, H. TiO_2/Si Composites Synthesized by Sol−Gel Method and Their Improved Electrode Performance as Li-Ion Battery Anodes. *Electrochim. Acta* **2013**, *111*, 575−580.
(27) Sakaguchi, H.; Toda, T.; Nagao, Y.; Esaka, T. Anode Properties of Lithium Storage Alloy Electrodes Prepared by Gas-Deposition. *Electrochem. Solid-State Lett.* **2007**, *10*, J146−J149.
(28) Usui, H.; Kiri, Y.; Sakaguchi, H. Effect of Carrier Gas on Anode Performance of Si Thick-Film Electrodes Prepared by Gas-Deposition Method. *Thin Solid Films* **2012**, *520*, 7006−7010.
(29) Ruiz, A. M.; Dezanneau, G.; Arbiol, J.; Cornet, A.; Morante, J. R. Insights into the Structural and Chemical Modifications of Nb Additive on TiO_2 Nanoparticles. *Chem. Mater.* **2004**, *16*, 862−871.
(30) Guidi, V.; Carotta, M. Effect of Dopants on Grain Coalescence and Oxygen Mobility in Nanostructured Titania Anatase and Rutile. *J. Phys. Chem. B* **2003**, *107*, 120−124.
(31) Yu, P.; Li, C.; Guo, X. Sodium Storage and Pseudocapacitive Charge in Textured $Li_4Ti_5O_{12}$ Thin Films. *J. Phys. Chem. C* **2014**, *118*, 10616−10624.
(32) Koudriachova, M. V.; Harrison, N. M.; de Leeuw, S. W. Density-Functional Simulations of Lithium Intercalation in Rutile. *Phys. Rev. B* **2002**, *65*, 235423−1−235423−12.

DOI: 10.1021/am508670z
ACS Appl. Mater. Interfaces 2015, 7, 6567−6573